# A climatology of thermodynamic vs. dynamic Arctic wintertime sea ice thickness effects during the CryoSat-2 era

James Anheuser[1], Yinghui Liu[2], and Jeffrey R. Key[2]

[1]Department of Atmospheric and Oceanic Sciences, University of Wisconsin-Madison, Madison, Wisconsin
[2]Center for Satellite Applications and Research, NOAA/NESDIS, Madison, Wisconsin

**Correspondence:** James Anheuser (anheuser@wisc.edu)

**Abstract.** Thermodynamic and dynamic sea ice thickness processes are affected by differing mechanisms in a changing climate. Independent observational datasets of each are essential for model validation and accurate projections of future sea ice conditions. Here we present the first long-term, sub-seasonal temporal resolution, basin-wide and Eulerian climatology of dynamically and thermodynamically driven sea ice thickness effects across the Arctic. Basin-wide estimates of thermodynamic growth rate are determined by coupling passive microwave retrieved snow–ice interface temperatures to a simple sea ice thermodynamic model, total growth is calculated from weekly Alfred Wegener Institute (AWI) CS2SMOS sea ice thickness spanning fall 2010 through spring 2021, and the dynamics component is calculated as their difference. The dynamic effects are further separated into advection and deformation effects using a sea ice motion dataset. Thermodynamic growth varies from less than 0.04 m wk$^{-1}$ in the central Arctic to greater than 0.08 m wk$^{-1}$ in the seasonal ice zones. High positive dynamic effects of greater than 0.04 m wk$^{-1}$, as high as twice that of thermodynamic growth, are found north of the Canadian Arctic Archipelago where the Transpolar Drift and Beaufort Gyre deposit ice. Strong negative dynamic effects of greater than 0.08 m wk$^{-1}$ are found where the Transpolar Drift originates, nearly equal to thermodynamic effects in these regions. Yearly results from the winter of 2019-2020 compare well with a recent study of the dynamic and thermodynamic effects on sea ice thickness along the Multidisciplinary drifting Observatory for the Study of Arctic Climate (MOSAiC) drift track during the winter of 2019-2020. Couplets of deformation and advection effects with opposite sign are common across the Arctic, with positive advection effects and negative deformation effects found in the Beaufort Sea and negative advection effects and positive deformation effects found in most other regions. The seasonal cycle shows deformation effect and overall dynamic effects increasing as the winter season progresses.

## 1 Introduction

Sea ice thickness is affected by processes that fall into two categories—thermodynamic and dynamic. Thermodynamic processes serve to increase or decrease thickness through phase change; dynamic processes serve to redistribute that thickness both horizontally and vertically. Sea ice models account separately for both thermodynamic and dynamic processes in order to determine ice thickness and predict how it will respond in a changing climate (Thorndike et al., 1975; Zhang and Rothrock, 2001; Hibler, 1980). These models are evaluated against sea ice thickness observations but current state of the art, basin-wide

25   observations capture only overall ice thickness (Markus et al., 2017; Laxon et al., 2013) and are unable to distinguish between thermodynamic and dynamic processes, which are independently affected through different mechanisms in a changing climate. In order to properly predict how sea ice will respond in a changing climate, these independent processes must be individually evaluated within models, requiring independent observations of each.

    The Multidisciplinary drifting Observatory for the Study of Arctic Climate (MOSAiC; Nicolaus et al., 2022) presented an

30   opportunity for partitioning thermodynamic and dynamic growth from a Lagrangian perspective along the Transpolar Drift over a full year from October 2019 to September 2020. von Albedyll et al. (2022) analyzed data from airborne electromagnetic (AEM) surveys and an ice mass balance buoy network to characterize the annual cycle of both dynamic and thermodynamic sea ice thickness contributions experienced by the ice pack surrounding the MOSAiC drift station. Thermodynamic growth was modeled using ice mass balance buoy temperature profiles and subtracted from overall ice growth captured by the airborne

35   electromagnetic survey data in order to calculate dynamic sea ice effects as a residual. Overall, the dynamics contribution of 0.1 m out of the 1.1 m growth amounts to 10%. Offering a potential window into basin–wide partitioning of thermodynamics versus dynamics, Koo et al. (2021) compared National Aeronautics and Space Administration (NASA) Ice, Cloud and Land Elevation Satellite (ICESat)-2 data collected over the MOSAiC drift station to ice mass balance buoy thicknesses collected during the field experiment. They found that the mode of ICESat-2 derived sea ice thickness over this region represented level

40   ice under the effects of thermodynamics only while mean and median sea ice thickness included sporadic deformation events which increased sea ice thickness under the effects of sea ice dynamics. Comparing the mean and median observations against the mode observations, the authors conclude that dynamics accounted for 35.6% of the mean sea ice thickness increase and 42.6% of the median sea ice thickness increase over a region enclosed by a 50 km radius around the Polarstern research vessel.

    Other studies used estimates of sea ice drift vectors to relate dynamics to sea ice thickness growth, again from a Lagrangian

45   perspective. Kwok and Cunningham (2016) calculated shear and divergence terms averaged over a region north of the Canadian Arctic Archipelago using estimated ice motion vectors during winter from 2011 through 2015. These terms and a constant thermodynamic growth term were linearly regressed to overall sea ice thickness change from European Space Agency (ESA) CryoSat-2. This analysis showed that divergence and shear led to 42% to 56% of overall thickness change averaged across the region in question during those winters, with the remaining change due to thermodynamic effects. The sea ice deformation

50   effects of a 2015 winter storm in the Transpolar Drift north of Svalbard were examined by Itkin et al. (2018), who analyzed AEM measurements of freeboard before and after the storm during the Norwegian Young Sea ICE (N-ICE2015) expedition. By tracking individual features in the measured sea ice distribution, they were able to relate divergence and shear to changes in sea ice deformation. In multiplying the effects of this single storm by the climatological average of ten to twenty storms per winter, the authors predict 5% to 10% volume increases due to deformation in the region. von Albedyll et al. (2021) also took

55   advantage of AEM freeboard measurements and satellite synthetic aperture radar observations of an unusually large polynya north of Greenland in 2018 to determine a relationship between deformation and thickness changes. Over the 65,000 km$^2$ polynya and over the 1 month of analysis, deformation of ice was found to account for an average of 50% of the thickness increase and in some cases as much as 90% of the thickness increase.

Kwok (2006) analyzed RADARSAT Geophysical Processor System (RGPS) sea ice motion vector derived Eulerian esti-
mates of deformation from 1996 to 2000 over a much larger area than the aforementioned studies, though independent of any
sea ice thickness measurements. They report that seasonal ice experiences more deformation than multi-year ice, possibly due
to its decreased thickness and strength. They also report a decrease in sea ice divergence as the winter growth season pro-
gresses, potentially via the same mechanism of increasing thickness and strength. Even without a link to sea ice thickness, the
findings of this study allow for the extrapolation of more localized, short term thickness effect results to a larger spatial scale.

While a number of localized and short term studies have yielded a partitioning of thermodynamic and dynamic growth, a
large scale and longer term dataset is lacking—especially from a Eulerian perspective for easier comparison to model outputs.
In this study we fill this knowledge gap by presenting the first long-term, sub-seasonal temporal resolution, basin-wide and
Eulerian estimation of dynamics effect on sea ice thickness, thermodynamic sea ice thickness growth, advection effect on sea
ice thickness and deformation effect on sea ice thickness. A difficulty inherent to large scale partitioning of thermodynamic and
dynamic effect has been large scale characterization of basal thermodynamic growth. The Stefan's Law Integrated Conducted
Energy (SLICE) retrieval methodology allows for daily and basin–wide retrieval of wintertime thermodynamic sea ice growth
rate using passive microwave brightness temperatures (Anheuser et al., 2022). Here, the retrieved thermodynamic growth rate
is used in conjunction with overall sea ice thickness changes from the radar altimeter aboard the European Space Agency
(ESA) CryoSat-2 satellite (Laxon et al., 2013) to estimate dynamic sea ice effects during the CryoSat-2 era beginning in 2010.
With overall sea ice thickness growth provided by a CryoSat-2 thickness product and thermodynamic growth provided by
SLICE, Arctic basin-wide sea ice thickness changes due to dynamics are calculated as the residual difference between the two.
The effects of advection are also estimated using a sea ice motion vector dataset allowing for the calculation of deformation
thickness as a residual of overall dynamic thickness effects and advection thickness effects.

## 2 Data

This analysis requires a sea ice thickness dataset, a sea ice motion estimation dataset and a thermodynamic sea ice growth
retrieval.

### 2.1 Satellite Sea Ice Thickness

Launched in 2010, the ESA CryoSat-2 satellite carries the SAR/Interferometric Radar Altimeter-2 (SIRAL-2) instrument
(Wingham et al., 2006; Laxon et al., 2013). In order to estimate sea ice thickness, altimetry data from the sensor is first
converted to freeboard—the distance between sea level and the top of the ice. The freeboard is then converted to sea ice
thickness with an assumed sea ice density and snow loading (Laxon et al., 2013). Gridded sea ice thickness products with
varying averaging periods, grid sizing and radar processing procedures are available from the Centre for Polar Observation and
Modelling (CPOM) (Tilling et al., 2018), the National Aeronautics and Space Agency (NASA) Goddard Space Flight Center
(GSFC) (Kurtz et al., 2014), the Alfred Wegener Institute (Ricker et al., 2014; Hendricks and Ricker, 2020; Ricker et al.,
2017a), the NASA Jet Propulsion Laboratory (Kwok and Cunningham, 2015), the ESA Climate Change Initiative (Hendricks

et al., 2018) and the Laboratoire d'Études en Géophysique et Océanographie Spatiales Center for Topographic studies of the Ocean and Hydrosphere (Guerreiro et al., 2017).

The ESA Soil Moisture and Ocean Salinity (SMOS) satellite, initially intended for measuring its namesake soil moisture and ocean salinity, carries the Microwave Imaging Radiometer using Aperture Synthesis (MIRAS) instrument. MIRAS measures

95    35 to 50+ km resolution passive microwave brightness temperatures at 1.4 GHz (Mecklenburg et al., 2012). At this frequency, the penetration depth into sea ice is high, allowing for retrieval of an ice temperature that can drive a radiative transfer model and yield an estimate of ice thickness (Tian-Kunze et al., 2014).

SIRAL-2 is an active instrument with a relatively small footprint, meaning it takes weeks for CryoSat-2 to cover the entire Arctic basin. On the other hand, SMOS covers the Arctic basin daily. Furthermore, uncertainties in SMOS sea ice thickness

100    measurements are lower than that of CryoSat-2 when measuring ice less than 0.5 m thick. These complementing characteristics create an opportunity for synergy between the satellites. The Alfred Wegener Institute (AWI) CS2SMOS sea ice thickness product takes advantage of this synergy (Ricker et al., 2017b). Through an optimal estimation scheme, the CS2SMOS dataset is available at a weekly time resolution and on a 25 km EASE-Grid 2.0. The dataset is particularly well suited for this study as it provides collocated weekly sea ice thickness observations of the entire basin—necessary for calculating basin–wide differences

105    on a weekly basis. Here we use weekly, wintertime CS2SMOS data from 2010 through 2021. Uncertainties in these data are discussed in Section 5.

## 2.2    Ice motion vectors

In order to estimate the effect of sea ice advection on sea ice thickness, the Polar Pathfinder Daily 25 km EASE-Grid Sea Ice Motion Vectors, Version 4 product from the NSIDC (Tschudi et al., 2019; Tschudi et al., 2020) was utilized. The product is

110    available from 1978 to present at daily and weekly temporal resolution. Ice motion vectors are estimated individually from cross correlated satellite brightness temperature data from the Advanced Microwave Scanning Radiometer (AMSR)-Earth Observing System (-E), Advanced Very High Resolution Radiometer (AVHRR), Scanning Multichannel Microwave Radiometer (SMMR), SSM/I and SSMIS, along with International Arctic Buoy Program (IABP) buoy locations, and a National Centers for Environmental Protection (NCEP)/National Center for Atmospheric Research (NCAR) wind reanalysis data derived free

115    drift estimate. These individual ice motion estimates are then merged via an optimal estimation scheme. Each data source is included only when available within the life span of the ice motion product, meaning sources vary throughout the record. Motion vectors are not available amongst the Canadian Arctic Archipelago. When compared against IABP buoy location data from between 1988 and 2011, DeRepentigny et al. (2016) found the weekly sea ice motion vectors to have a 7% median error.

## 2.3    Stefan's Law Integrated Conducted Energy

120    The SLICE methodology drives Stefan's Law (Stefan, 1891; Lepparanta, 1993) with snow–ice interface temperature retrieved with passive microwave brightness temperatures (Kilic et al., 2019) in order to retrieve instantaneous thermodynamic sea ice

thickness growth rate. Stefan's Law of simple sea ice thermodynamics states that:

$$f(t, H, \mathbf{x}) = \frac{\kappa_{eff}}{\rho_i L H}\left(T_f - T_{si}\right) - \frac{F_w}{\rho_i L}, \tag{1}$$

where $f(t, H, \mathbf{x})$ is the thermodynamic growth rate, $\rho_i$ is the density of sea ice, $L$ is the latent heat of fusion, $\kappa_{eff}$ is the

125 effective thermal conductivity of sea ice, $H$ is sea ice thickness, $T_f$ is the freezing point of sea water, $T_{si}$ is the snow–ice interface temperature, and $F_w$ is basal heat flux from the liquid sea water to the solid sea ice. Latent heat of fusion and effective thermal conductivity are calculated using a set of equations that accounts for the multi-phase properties of sea ice (Feltham et al., 2006). In the present analysis, sea ice thickness is taken from the CS2SMOS thickness field, sea ice density is taken to be 917 kg m$^{-3}$, and basal flux is a constant 2 W$^{-2}$. SLICE is available daily and basin-wide but does carry three assumptions—

130 heat conduction in the horizontal direction is assumed to be negligible, it is assumed that there is no thermal inertia present in the ice, and it is assumed that there is no internal heat source, such as the absorption of short wave radiation. These assumptions and the snow–ice interface temperature retrieval are only valid during winter, constraining the analysis to 1 November through 31 March. More information regarding SLICE can be found in Anheuser et al. (2022).

## 3   Methods

135 Sea ice thickness is affected by thermodynamic processes and dynamic processes. Thermodynamic processes serve to change sea ice thickness through molecular phase change and dynamic process serve to change local sea ice thickness through the mechanical processes of advection and deformation (ridging or lead formation). An Eulerian governing equation for sea ice thickness sums thermodynamic and dynamic processes:

$$\frac{\partial H}{\partial t} = f(t, H, \mathbf{x}) - \nabla \cdot (\mathbf{u}H), \tag{2}$$

140 where $H$ is plane slab sea ice thickness, $t$ is time, $f$ is a function of time, thickness and position vector $\mathbf{x}$ describing thermodynamic sea ice thickness increase, and $\mathbf{u}$ is the ice motion vector. The second term on the right hand side represents dynamic sea ice thickness processes.

We aimed to partition basin-wide observations of overall changes to the sea ice thickness field, $\frac{\partial H}{\partial t}$, into component parts of thermodynamic growth, $f(t, H, \mathbf{x})$, and dynamic effects, $-\nabla \cdot (\mathbf{u}H)$. The result is basin-wide observations of thermodynamic

145 and dynamic process effects on sea ice thickness. At each weekly time step, $\frac{\partial H}{\partial t}$ was calculated as the difference between the CS2SMOS sea ice thickness field from the current time step and that from the following time step. We estimated dynamics, $-\nabla \cdot (\mathbf{u}H)$, as the difference between total growth, $\frac{\partial H}{\partial t}$, and expected thermodynamic growth, $f(t, H, \mathbf{x})$, retrieved using the SLICE methodology using the CS2SMOS sea ice thickness as the initial thickness.

The dynamics term within Eq. 2 can be further decomposed to form:

150 $$\nabla \cdot (\mathbf{u}H) = (\nabla H) \cdot \mathbf{u} + H(\nabla \cdot \mathbf{u}), \tag{3}$$

where the first term on the right now represents changes to local sea ice thickness due to advection, i.e., the movement of ice transporting ice of a new thickness into a grid cell, and the second term on the right represents sea ice thickness changes due

to deformation processes caused by the divergence or convergence of the ice motion vector field. Deformation effect does not include advection and therefore can be considered Lagrangian dynamics—i.e., the dynamic effect as observed by a Lagrangian drifter. As the dynamics term can be divided into components, so to can dynamic effect estimates. Estimates of dynamic effects were further partitioned into advection effects and deformation effects using the sea ice motion vector product. At every time step, the first term on the right hand side of Eq. 3 is calculated using the CS2SMOS ice thickness field and sea ice motion vectors and is taken to be advection effect. The deformation effect is in turn taken to be the residual difference of the dynamic effect and this advection effect. This approach was taken over calculating the deformation effect using the motion vectors and advection effect as a residual because the motion vectors themselves were found to be more reliable than the divergence of these motion vectors. As motion vectors are not available within the Canadian Arctic Archipelago, advection effects and deformation effect estimates are not available in this region either.

In summary, the governing equation expressed in Eq. 2 is conceptually reconstructed as follows:

$$\frac{\partial(CS2SMOS)}{\partial t} = SLICE + dynamic\ effect, \tag{4}$$

and the dynamic effect is further decomposed into advection and deformation effects with Eq. 3 conceptually reconstructed as follows:

$$dynamic\ effect = (\nabla CS2SMOS_i) \cdot ice\ motion\ vector\ + deformation\ effect. \tag{5}$$

The results shown here are weekly integrations of the terms within Eqs. 4 and 5. The dataset covers 1 November through 1 April, due to SLICE assumptions described in Section 2.3 and availability of CS2SMOS data, spanning the ten winters beginning in the years 2010 and 2012-2020. The 2010 data begins on 15 November rather than 1 November along with the availability of CryoSat-2 data and the winter beginning in 2011 is not included due to a gap between availability of passive microwave data from the earlier AMSR-E and later AMSR2. At each weekly time step, $i$, the following steps were completed at each point on the 25 km EASE-Grid 2.0:

1. $\frac{\partial(CS2SMOS)}{\partial t} = CS2SMOS_{i+1} - CS2SMOS_i$

2. $thermodynamic\ growth = SLICE$

3. $dynamic\ effect = \frac{\partial(CS2SMOS)}{\partial t} - SLICE$

4. $advection\ effect = (\nabla CS2SMOS_i) \cdot ice\ motion\ vector$

5. $deformation\ effect = dynamic\ effect\ - advection\ effect$

## 4 Results

Figure 1 shows the wintertime mean dynamic effect, thermodynamic effect, advection effect and deformation effect on sea ice thickness across the entire 10 year analysis period. The magnitude and sign of these terms varies across the Northern

Hemisphere sea ice. As expected, thermodynamic thickness growth is highest in the seasonal ice zones, often greater than 0.08 m wk$^{-1}$, and inversely proportional to the climatological sea ice thickness, leading to less than 0.04 m wk$^{-1}$ of thermodynamic growth in much of the Central Arctic. Dynamic effects increase sea ice thickness over 29% of the area exhibiting ice during the

185 study period and decrease sea ice thickness over the remaining area. An increase in sea ice thickness due to dynamics occurs off the Siberian Coast in the Chukchi Sea where the Beaufort Gyre tends to deposit advected ice and similarly north the of Canadian Arctic Archipelago where both the Beaufort Gyre and Transpolar Drift tend to deposit advected ice. The highest positive dynamic effects of greater than 0.04 m wk$^{-1}$ occurs just north of the central Canadian Arctic Archipelago. A decrease in sea ice thickness due to dynamics, often with magnitude greater than 0.08 m wk$^{-1}$, occurs in the coastal regions of the

190 Kara and Laptev Seas from where the transpolar drift tends to remove ice, and similarly in the coastal regions of the Beaufort Sea due to a similar effect of the Beaufort Gyre. The negative advection effect dominates the Arctic sea ice, covering 66% of the study area. The exception primarily occurs where the Beaufort Gyre advects thick ice from north of the Canadian Arctic Archipelago to the Beaufort Sea. Here, advection effects greater than 0.04 m wk$^{-1}$ are found. The most significant negative advection effects, less than 0.04 m wk$^{-1}$, occur in coastal Laptev Sea. Similar to advection effects, deformation effects are

195 negative over most of the Arctic, covering 62% of the study area. The largest deformation effects of greater than 0.04 m wk$^{-1}$ occur where the ice motion tends to deposit and form ice ridges, north of the central Canadian Arctic Archipelago, in the Chukchi Sea and north of Greenland. The Barents and Kara Seas are dominated by strong negative deformation effects, often times with magnitudes greater than 0.08 m wk$^{-1}$. Coupled with the positive advection effects in the Beaufort Sea are negative deformation effects in this region.

200 In the Fram Strait and Baffin Bay, dynamics serve to deposit ice on the east coast of Baffin Island and Greenland. Thermodynamic growth is high in Baffin Bay as ice is produced and exported by the prevailing ice drift. Advection in Baffin Bay clearly reduces thickness in the northern portions of the region as the current transports ice from the north to the southern portion, where advection increases ice thickness. Deformation shows that some ice is deposited and ridged on the east coast of Baffin Island. A very high advection effect is shown in the East Greenland Sea where ice export is substantial. Deformation effects

205 are strongly negative here as the ice likely experiences lead formation throughout its export through the Fram Strait.

Uncertainty in the climatological mean is characterized using standard error of the mean and shown in Fig. 2. Standard error is calculated as the standard deviation of all dynamic effect measurements at a given grid cell divided by the square root of the number of data points at that grid cell:

$$\sigma_{\bar{E}} = \frac{\sigma_E}{\sqrt{N}}, \tag{6}$$

210 where $\sigma_E$ is the standard deviation of the effect in question and N is the number of data points. Generally, standard error increases with a decrease in latitude for all four thickness effects. With regard to the dynamics and deformation plots, this is likely due to a decrease in CryoSat-2 satellite overpasses and increase in thickness variability and coastal interference in the lower latitudes leading to higher uncertainties in the CS2SMOS sea ice thickness product. Thermodynamic effect standard error is lowest in the central Arctic where thermodynamic growth rates themselves are also quite low. Advection effects standard
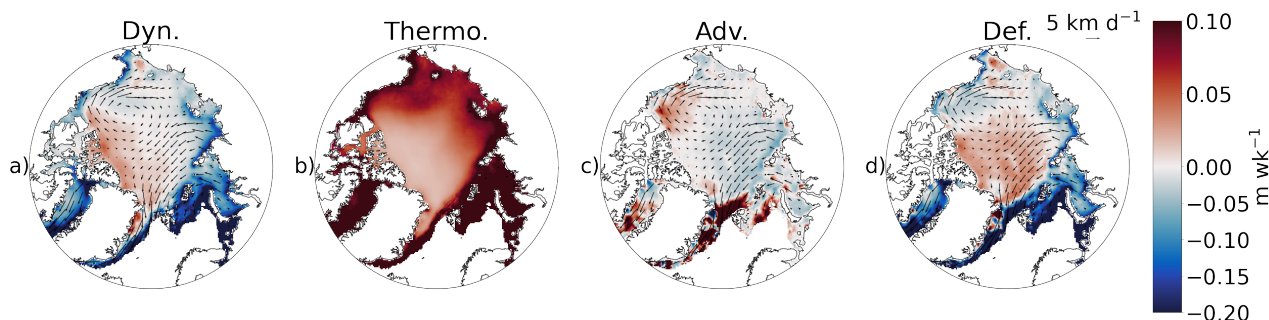
**Figure 1.** Wintertime mean from late 2010 through early 2021 (except the winter of 2011-2012) sea ice thickness changes due to a) dynamic effects, b) thermodynamic effects, c) advection effects and d) deformation effects. Mean sea ice motion vectors from the same period are also plotted with a), c) and d). The dynamic effect, advection and deformation follow spatial patterns evident in the ice motion vectors.

215   error is highest in the East Greenland, Barents and Kara Seas, where motion vectors are largest and most variable. In general, uncertainty is significant in the Kara, Barents and East Greenland Seas as well as most coastal regions.
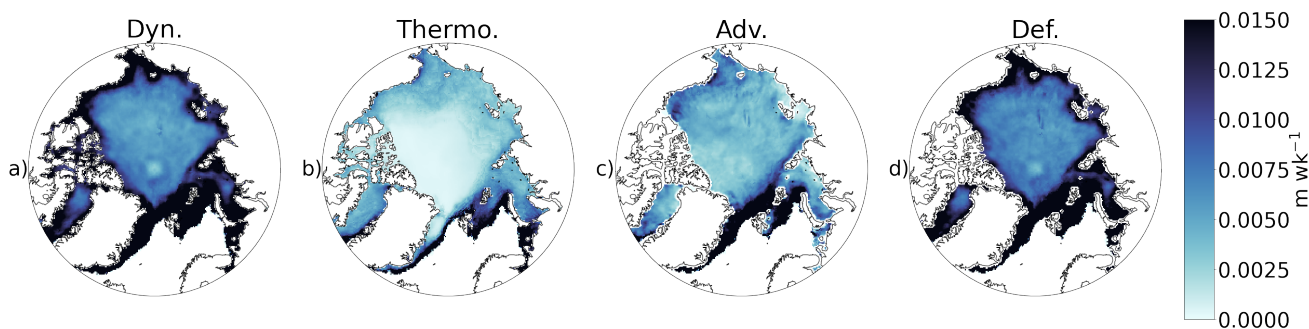
**Figure 2.** Uncertainty calculated as standard error for each grid cell during wintertime from late 2010 through early 2021 (except the winter of 2011-2012) sea ice thickness changes due to a) dynamic effects, b) thermodynamic effect, c) advection effect and d) deformation effect. Uncertainty increases with a decrease in latitude as the number of weeks with ice cover decreases.

Regional mean values across the analysis period for each effect are summarized in Table 1. Regional extent and location are shown in Fig. 3 and are defined per Meier et al. (2007). Thermodynamic growth is highest in regions with the lowest mean thickness, as expected by Eq. 1. The regional mean values of the dynamics, advection and deformation effects are all skewed

220   downward by small, coastal sub-regions that exhibit very large negative thickness effects. In order to remove these effects, regional mean values excluding all grid cells within 200 km of a coast are shown in parenthesis. The strongest dynamic effect is exhibited in the Barents Sea, where the mean dynamic effect is -0.269 m wk$^{-1}$ and -0.222 m wk$^{-1}$ with coastal regions excluded, the bulk of which is made up of the deformation effect at -0.289 m wk$^{-1}$ and -0.263 m wk$^{-1}$ with coastal regions excluded. This region also has the thinnest ice at 0.259 m and greatest thermodynamic growth of 0.257 m wk$^{-1}$. Mean dynamic

225   effects are negative for every region except the central Arctic, where mean dynamic effects across the region are negligible.

Notably, removal of coastal areas from the Laptev Sea decreases the magnitude of negative dynamic effect from 0.060 m wk$^{-1}$ to 0.029 m wk$^{-1}$ and in the Chukchi Sea, where both strong negative and strong positive dynamic effects are present, from 0.024 m wk$^{-1}$ to 0.008 m wk$^{-1}$. Advection effects are small in all regions, all less than 0.021 m wk$^{-1}$ in magnitude except in the East Greenland Sea where advection via ice export through the Fram Strait increases mean thickness by 0.113 m wk$^{-1}$.

230 The advection effect is negative in all other regions except Baffin Bay and the Barents and Beaufort Seas which exhibit mean advection effects of 0.010 m wk$^{-1}$, 0.013 m wk$^{-1}$ and 0.014 m wk$^{-1}$, respectively. The deformation effect magnitude is largest in Baffin Bay and the East Greenland and Barents Seas by a significant margin, at -0.251 m wk$^{-1}$, -0.247 m wk$^{-1}$ and -0.289 m wk$^{-1}$, respectively. The remaining regions experience mean deformation effects that are at most 0.090 m wk$^{-1}$ in magnitude and all negative, with the notable exception of the Central Arctic with a mean deformation effect of 0.008 m wk$^{-1}$.

235 As with total dynamic effect, removal of coastal areas reduced the magnitude of negative deformation effect in the Laptev Sea, from 0.038 m wk$^{-1}$ to 0.007 m wk$^{-1}$.
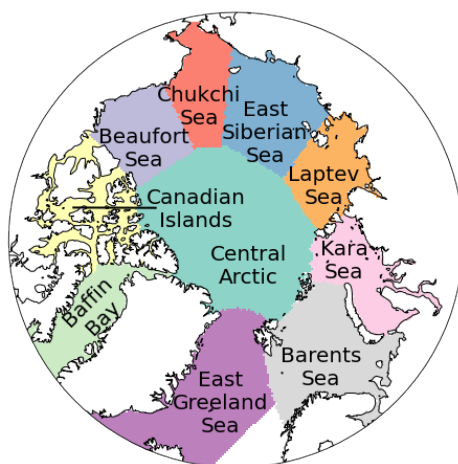
**Figure 3.** Location, extent and corresponding name of regions used in Table 1.

The mean advection and deformation fields show interesting patterns relative to the Beaufort Gyre and Transpolar Drift. North of the western portion of the Canadian Arctic Archipelago, the Beaufort Gyre advects thicker ice into the Beaufort Sea, leading to a increase in sea ice thickness in the region. As this ice is advected further west by the gyre in the Beaufort Sea,

240 it experiences a decrease in thickness due to deformation via lead formation by divergence in the flow. This ice continues to be advected through the Chukchi Sea and into the East Siberian Sea. The positive advection effect decreases in these regions however, as deformation has reduced the mean thickness of this ice, resulting in advection of thinner ice. The deformation effect in these regions is, however, positive, as the flow pattern deposits ice and leads to ridging, increasing the over sea ice thickness. The poleward leg of the Beaufort Gyre and Transpolar Drift are characterized by negative advection effects and

245 positive deformation. In contrast to the westward leg of the Beaufort Gyre, the flow pattern in these regions is from thin ice

**Table 1.** Regional mean thickness, dynamic effect, thermodynamic effect, advection effect and deformation effect on thickness. Regional mean with 200 km from coastlines removed is shown in parenthesis.

| Region | Thickness [m] | Dynamics [m wk$^{-1}$] | Thermo. [m wk$^{-1}$] | Advection [m wk$^{-1}$] | Deformation [m wk$^{-1}$] |
|---|---|---|---|---|---|
| Baffin Bay | 0.383 (0.308) | -0.237 (-0.263) | 0.240 (0.264) | 0.010 (0.025) | -0.251 (-0.290) |
| East Greeland Sea | 0.905 (0.863) | -0.121 (-0.145) | 0.140 (0.145) | 0.113 (0.145) | -0.247 (-0.316) |
| Barents Sea | 0.259 (0.292) | -0.269 (-0.222) | 0.257 (0.234) | 0.013 (0.027) | -0.289 (-0.263) |
| Kara Sea | 0.664 (0.698) | -0.104 (-0.090) | 0.130 (0.122) | -0.013 (-0.014) | -0.090 (-0.077) |
| Laptev Sea | 0.992 (1.123) | -0.060 (-0.029) | 0.095 (0.074) | -0.021 (-0.022) | -0.038 (-0.007) |
| East Siberian Sea | 1.192 (1.244) | -0.018 (-0.011) | 0.070 (0.064) | -0.008 (-0.008) | -0.010 (-0.003) |
| Chukchi Sea | 1.051 (1.132) | -0.024 (-0.008) | 0.086 (0.074) | -0.007 (-0.003) | -0.015 (-0.005) |
| Beaufort Sea | 1.424 (1.468) | -0.009 (0.000) | 0.061 (0.051) | 0.014 (0.019) | -0.022 (-0.019) |
| Canadian Islands | 1.452 (-) | -0.027 (-) | 0.075 (-) | - (-) | - (-) |
| Central Arctic | 2.105 (2.063) | -0.000 (0.001) | 0.034 (0.031) | -0.009 (-0.012) | 0.008 (0.012) |
| Entire Arctic | 1.356 (1.380) | -0.032 (-0.040) | 0.072 (0.076) | -0.003 (0.003) | -0.028 (-0.045) |

towards thicker ice. This leads to a negative advection effect accompanied by a positive deformation effect due to ridging. The advection and deformation effects sum to a slightly positive dynamic effect here. The coastal regions of the Kara and Laptev Seas experience negative effects from both advection and deformation. These broad patterns are reinforced by the yearly data show in Fig. A1, which illustrates the effects that the location and strength of the Beaufort Gyre have on the advection and
250 deformation fields on a yearly basis.
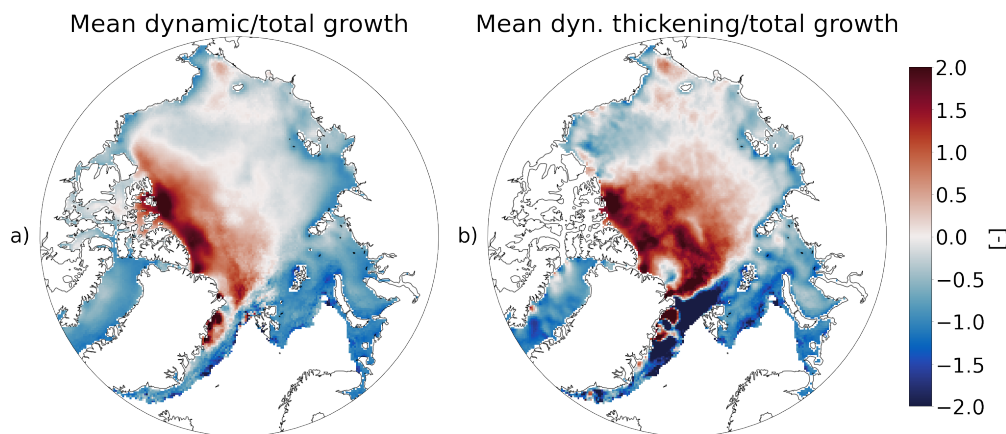
**Figure 4.** Wintertime mean from late 2010 through early 2021 (except the winter of 2011-2012) relative impact of a) dynamic effects over thermodynamic sea ice thickness growth and b) deformation (excluding advection) over thermodynamic sea ice thickness growth. Alternatively, the figure can be viewed as a) Eulerian dynamics and b) Lagrangian dynamics.

Fig. 4 shows mean dynamics and mean deformation in relative terms as ratios to thermodynamic growth. These plots look similar to those in in Fig. 1 as the scaling quantity, thermodynamic growth, is fairly uniform across most of the Arctic. Nevertheless, the relative importance of dynamics to thermodynamic growth is an important result. Much of the Arctic shows a slightly negative impact of total dynamics relative to thermodynamic growth. The areas north of the Canadian Arctic Archipelago and

255  Greenland show the highest relative impact of dynamics, with some regions showing dynamics with twice the impact relative to thermodynamics. The coastal regions of the Kara and Laptev Seas show significant negative impacts of dynamics, with magnitudes nearly equal to thermodynamics. The greatest relative importance of deformation is also found in the regions north of the Canadian Arctic Archipelago and Greenland, though skewing more towards the central Arctic. In these regions deformation effects can be twice that of thermodynamics. The largest positive relative impact of deformation is found between Svalbard

260  and Greenland where the Transpolar Drift causes ridging in thick ice that isn't experiencing large thermodynamic growth.
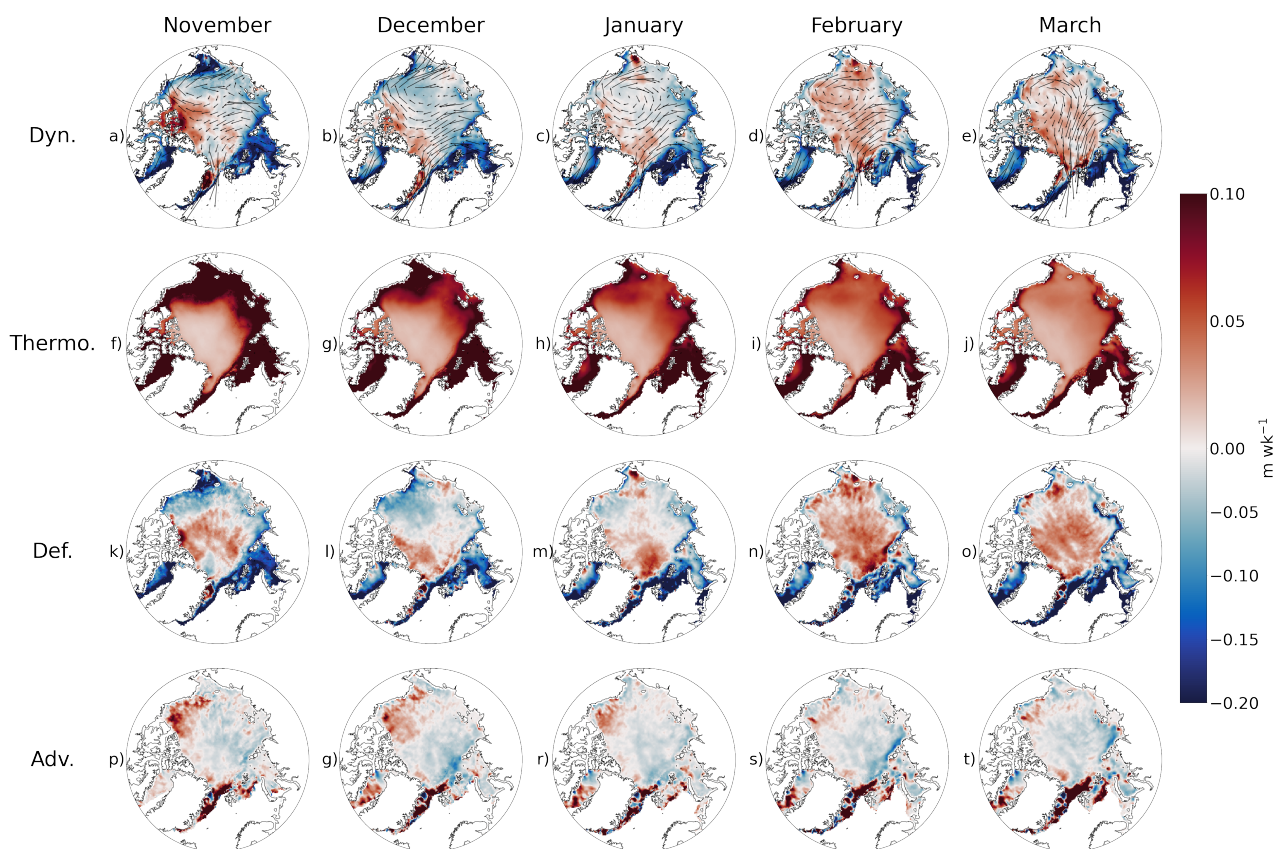
**Figure 5.** Monthly mean a-e) dynamic effect, f-j) thermodynamic effect, k-o) deformation effect, and p-t) over the analysis period. Dynamic and deformation effects increase through the growth season.

Fig. 5 shows the monthly mean overall dynamic effect, thermodynamic growth, deformation effect and advection effect across the ten winters of data. The monthly deformation fields depict a negative deformation effect in the westward leg of

the Beaufort Gyre that peaks in December, decreases in January and is nearly absent in February and March. February and March do, however, depict deformation maxima north of Svalbard and Eastern Siberia. Positive advection of ice thickness by the Beaufort Gyre similarly peaks in the early winter, though the broad pattern of the advection field remains consistent throughout the winter. The deformation and advection fields sum to an overall dynamic effect that increases with time in winter, dominated by the deformation effect. The thermodynamic growth field, inversely proportional to sea ice thickness, remains consistently low across the Central Arctic through most of the winter and higher in the perennial ice zones, though growth decreases as thickness increases with time in these areas.
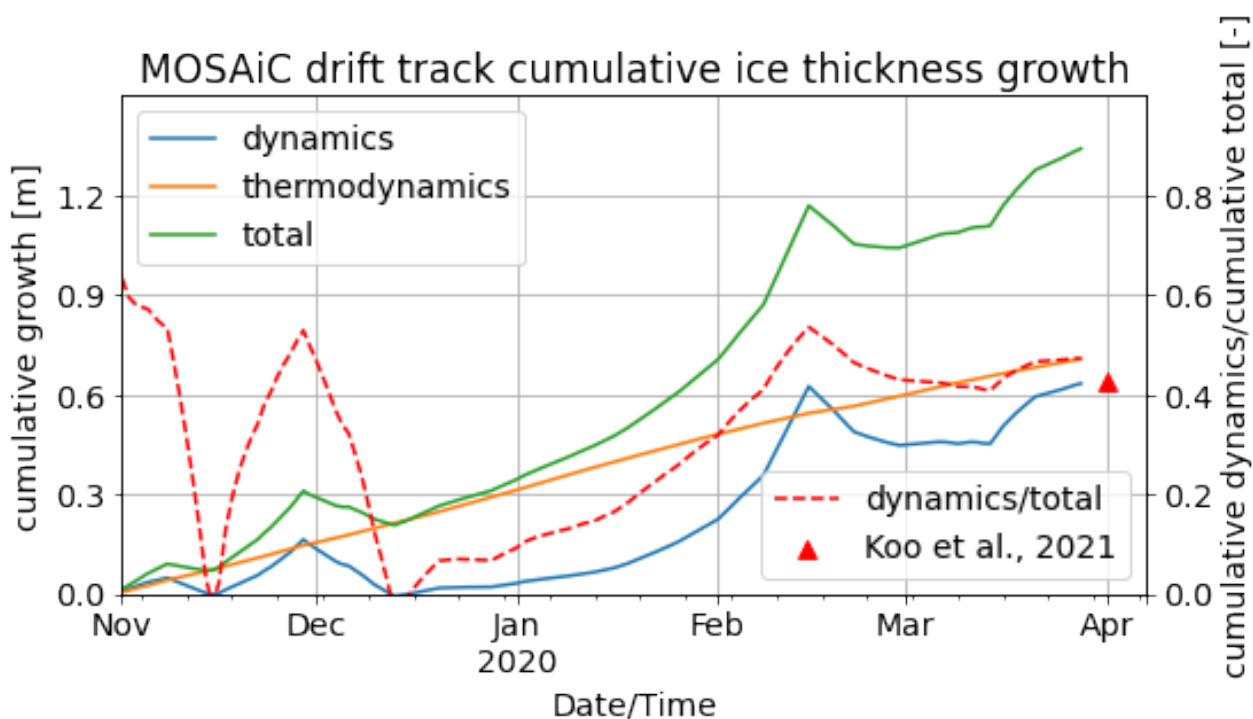
**Figure 6.** Cumulative dynamic, thermodynamic and total sea ice thickness growth (primary vertical axis) and cumulative dynamic over cumulative total sea ice thickness growth (secondary vertical axis) along the MOSAiC drift track. The red triangle represents cumulative dynamics over cumulative total growth over a similar area reported by Koo et al. (2021) who used ICESat-2 to determine dynamics vs. thermodynamics along the MOSAiC drift track. Dynamics accounts for nearly half of all thickness growth by 1 April 2020.

The cumulative effects of deformation, i.e., Lagrangian dynamics, thermodynamics and their sum and relative magnitudes as experienced by the grid cell nearest to the MOSAiC drift station at each time step, are depicted in Fig. 6 in order to compare these results with those reported by von Albedyll et al. (2022) and Koo et al. (2021). The analysis period is 1 November 2019 through 1 April 2020. Thermodynamic growth during the period is steady and consistent, ranging between $3.0 \times 10^{-3}$ m d$^{-1}$ and $6.0 \times 10^{-3}$ m d$^{-1}$. Cumulative thermodynamic growth at the end of the period is 0.71 m. As expected, dynamic effects were much more variable, ranging from $-2.1 \times 10^{-2}$ m d$^{-1}$ to $3.9 \times 10^{-2}$ m d$^{-1}$. Dynamic effect maxima occurred in

November and February and has a cumulative total of 0.63 m at the end of the period. Total growth steadily rises due to the thermodynamic component and follows the shape of the dynamics component, with local peaks in November and February. The highest cumulative growth of 1.34 m is found at the end of the period. As a percentage of total growth, dynamics ends the season at 47.2% of the total growth. Over a similar study area, Koo et al. (2021) found dynamics to account for 42.6% of mean
280   total growth.

## 5   Discussion

The climatology of ice motion during the CryoSat-2 era as plotted in Fig. 1 suggests the patterns of dynamic effect demonstrated here are sound. The Beaufort Gyre and Transpolar Drift both transport ice towards the Canadian Arctic Archipelago, where ridging causes both high positive dynamic effect and high positive deformation effect. Where the Transpolar Drift originates,
285   in the coastal region of the Laptev Sea, strong negative dynamic and deformation effects dominate. Between these regions and the Canadian Arctic Archipelago, a couplet of negative advection effect and positive deformation effect characterizes a region where the Transpolar Drift tends to move thinner ice towards thicker ice, all the while experiencing ridging and other effects that increase thickness. Where the motion vectors show the Beaufort Gyre transporting ice westward from north of the Canadian Arctic Archipelago, a similar but reversed couplet of high positive advection effect and strong negative deformation
290   effect is found. The ice is transported from a region of climatologically thicker ice north of the Canadian Arctic Archipelago to a region of climatologically thinner ice in the Beaufort Sea, leading to a positive advection effect. In this same region, the Beaufort Gyre flow pattern is diverging and accelerating westward. This divergence leads to lead formation and a reduction in mean overall thickness, as reflected by negative deformation effects in this region. This matches previous work suggesting high divergence and lead formation in this region (Kwok, 2006; Willmes and Heinemann, 2016; Hoffman et al., 2019). As this
295   ice is further advected westward around the Beaufort Gyre, the advection and deformation effects return to near zero and some ice is deposited north of Eastern Siberia where ridging leads to positive dynamic and deformation effects. The location and magnitude of these patterns varies year to year with sea ice flow patterns and likely atmospheric conditions as demonstrated in Fig. A1.

   Kwok (2006) reported on the spatial and seasonal characteristics of Arctic sea ice deformation in the ice motion vector fields
300   using high resolution RGPS data from 1997-2000. Though the years in question do not overlap with the analysis period shown here, their results offer context for understanding dynamic sea ice effects. Their analysis showed divergence in the Beaufort Sea and convergence north of eastern Siberia, a pattern reflected here by negative deformation effects and positive deformation effects in those same regions, respectively. They show that the fraction of deformed ice in these regions decreases over the course of the growth season, a phenomenon also shown by a lessening of the negative deformation effects from November
305   through March in Fig. 5. The ice motion vectors used here are not suited for vector calculus calculations of deformation terms but a future comparison between concurrent observations of vector deformation fields and dynamics would be fruitful for model improvement.

The mean relative dynamic effect over total growth shown in Fig. 4 is useful for understanding the relative importance of dynamics and deformation and is useful for eventual comparison across time periods. The highest relative impact of dynamics is found north of the Canadian Arctic Archipelago where the Beaufort Gyre and Transpolar Drift both deposit ice and thermodynamic growth is limited due to the high thickness of the ice. The relative deformation plot tells a different story. With advection removed, this plot shows that a drifting observer would experience strong negative deformation effects relative to thermodynamic growth in the Beaufort Sea and increasingly strong positive deformation effects relative to thermodynamics in the Transpolar Drift and eastward leg of the Beaufort Gyre. Whereas many regions experience less than 25% relative impact of overall dynamics, few areas experience such a low impact of deformation. In the areas of low relative dynamic impact, advection nearly cancels this deformation. In the areas north of the Canadian Arctic Archipelago, both dynamics and deformation make up between 25% and 75% of total growth, consistent with Kwok and Cunningham (2016) who report 42%-56% of mean thickness change is due to deformation.

Within the methodology used here, the dynamic effects term represents Eulerian dynamics–i.e., a spatially stationary observer of sea ice thickness would observe changes due to thermodynamics and changes captured by the dynamics term, which includes advection. A Lagrangian observer, whom is advecting as described by sea ice motion vector, would not experience changes due to this advection. The Lagrangian observer would only experience changes due to the deformation in the framework here. In this way, our Eulerian deformation term can be considered Lagrangian dynamics. Two Lagrangian studies of dynamics observed along the MOSAiC drift track offer useful context for validating our Eulerian results (von Albedyll et al., 2022; Koo et al., 2021). The comparison is necessarily between our weekly Eulerian deformation term—i.e., Lagrangian dynamics—from closest in space and time to the MOSAiC drift track and dynamics as described within those studies.

von Albedyll et al. (2022) reported 10% dynamic sea ice thickness growth relative to total growth along the MOSAiC drift, lower than the lower than the 48.7% reported here and the 42.6% reported by Koo et al. (2021). A likely primary cause of this discrepancy is related to temporal resolution. von Albedyll et al. (2022) analyzed AEM sea ice thickness distributions across the 50 km buoy network at the beginning of the growth season and at the end of the growth season, estimating a cumulative thermodynamic growth during the season using buoy thicknesses. Through a phenomenon acknowledged by the authors, this does not account for dynamics affecting thermodynamic growth throughout the growth season. If dynamics were to increase thickness, as our results and those reported by Koo et al. (2021) show did indeed occur along the MOSAiC drift track, thermodynamic growth rate would decrease as shown in Eq. 1. Without accounting for this effect, thermodynamic growth is overestimated and dynamically driven growth is underestimated, due to the later being calculated as a residual. The higher temporal resolutions in this work and Koo et al. (2021) greatly improve—though do not eliminate—this issue. Indeed, von Albedyll et al. (2022) report a cumulative thermodynamic growth of 1 m, whereas we report total thermodynamic growth of 0.7 m. This is significant, especially given von Albedyll et al. (2022) measured growth between 14 October and 17 April, whereas our analysis period is from 1 November to 1 April (this time discrepancy alone may cause differences as well).

Another potential reason for discrepancy between our results and those of von Albedyll et al. (2022) is the higher overall thickness growth measured by CryoSat-2 relative to the AEM measurements. We report a total mean growth along the MOSAiC drift track of 1.3 m relative to 1.1 m from the AEM survey. Indeed, CS2SMOS shows a mean sea ice thickness of 2.52 m on 1

April 2020 at the MOSAiC location relative to 2.2 m from the AEM surveys. This would manifest as an increase in dynamic effect in our analysis, as dynamics is calculated as a residual when thermodynamics are subtracted from total growth. That
345 there are differences here is not surprising. The satellite measurements are gridded and taken from the nearest grid cell to MOSAiC, while the AEM surveys are centered on the MOSAiC buoy array. On the other hand, though the AEM has higher spatial resolution, the coverage over the 50 km buoy network is not complete. The satellite samples a larger area, although not centered exactly on the MOSAiC buoy array. That our results agree better with Koo et al. (2021) is not surprising, given both studies have used satellite sea ice thickness as the primary dataset. Given that our study aims at a temporally and spatially
350 larger scale while these studies are more focused on singular drift track, we can expect differences in results while using these more localized studies to provide context for our larger scale study.

The calculations and analyses carried out here are all performed using satellite data on a 25 km EASE-Grid 2.0. Whereas sea ice processes can occur on much smaller scales, the results on satellite scale are useful for deciphering patterns and trends on an Arctic basin-wide basis. The CS2SMOS sea ice thickness dataset represents mean sea ice thickness within each grid
355 cell. In actuality, thickness over the grid cell is defined by a distribution rather than a single value. However, without having observed local thickness distributions available at each time step, we have omitted thickness distributions and applied the SLICE retrieval using the mean thickness provided by CS2SMOS. It is likely that implementing thickness distributions would augment our results. Given the non-linear and inverse relationship between thickness and thermodynamic growth rate present in Eq. **??**, a distribution favoring ice thinner than the mean thickness over that thicker than the mean within a grid cell would
360 increase thermodynamic growth and decrease dynamic effects (and vice versa). Though snow–ice interface temperature is not expected to vary as greatly as sea ice thickness across a 25 km grid cell, passive microwave snow–ice interface temperature retrieval also represents the mean across each grid cell. The dynamic, thermodynamic, advection and deformation effects then necessarily represent mean effects over the grid cell area. While few areas within a grid cell will have experienced exactly the effects described by our results, the cell will have experienced these effects on the mean. A useful corollary to imagine these
365 effects to be total volumetric changes within each cell.

The largest source of uncertainty is that from the AWI CS2SMOS sea ice thickness product. The AWI CS2SMOS product merges sea ice thickness retrievals from CryoSat-2 and SMOS into a product that contains reduced uncertainties relative to each instrument's products independently (Ricker et al., 2017b). CryoSat-2 uncertainties are highest over thin ice while SMOS uncertainties are highest over thick ice, creating the opportunity for synergy. CryoSat-2 uncertainties are made up of
370 observational uncertainties or noise and systemic uncertainties or bias (Ricker et al., 2014). Observational uncertainties are reduced through spatial averaging on the grid and optimal estimation methodology used to create the CS2SMOS product. While systemic uncertainties effect estimates of absolute thickness, differencing of thickness between time steps removes them from the estimations of various thickness effects calculated in this work. SMOS uncertainties are caused by uncertainties in the input parameters to the energy budget used to estimate sea ice thickness and are especially high over MYI, results from
375 which are removed from the optimal interpolation. The AWI CS2SMOS product provides an uncertainty value including these effects for each individual estimate at each time step and grid cell. Figure 7 shows a standard error and relative standard error calculated using a mean of this uncertainty and mean ice thickness across the study time period and area. The magnitudes of

this mean uncertainty range from 0.005 m to 0.01 m and increases with a decrease in latitude, with some regions experiencing a mean uncertainty of 0.015 m and greater. Relative uncertainty is below 5% across most of the study area. The overall
380    CS2SMOS sea ice thickness observational uncertainty effects uncertainty in all four calculated effects. The thermodynamic effect is affected via the presence of sea ice thickness, $H$, in Eq. 1. Relative uncertainty due to this term is equal to the relative uncertainty of this term itself and mostly less than 5%, as shown in Fig. 7b. The thermodynamic component is also affected by any systemic bias present in the CS2SMOS product. The dynamic effect is calculated as a residual of thermodynamics and overall thickness change. The mean uncertainty shown in Fig. 7a is very similar to the uncertainty of the dynamic effect
385    as shown in Fig. 2, lending credibility to these uncertainty estimates. The ratio of mean dynamic effect over thermodynamic growth, shown in Fig. 4, is particularly sensitive to uncertainty or bias in the CS2SMOS product. An underestimation of sea ice thickness would lead to overestimation of thermodynamic growth and underestimation of dynamic effect, altering both the numerator and denominator of the ratio of the two. The advection term is also affected by the CS2SMOS thickness uncertainty as it is calculated using a spatial gradient of the thickness field. The deformation term is affected by the CS2SMOS uncertainty
390    as it is calculated as the difference between overall dynamics and advection.
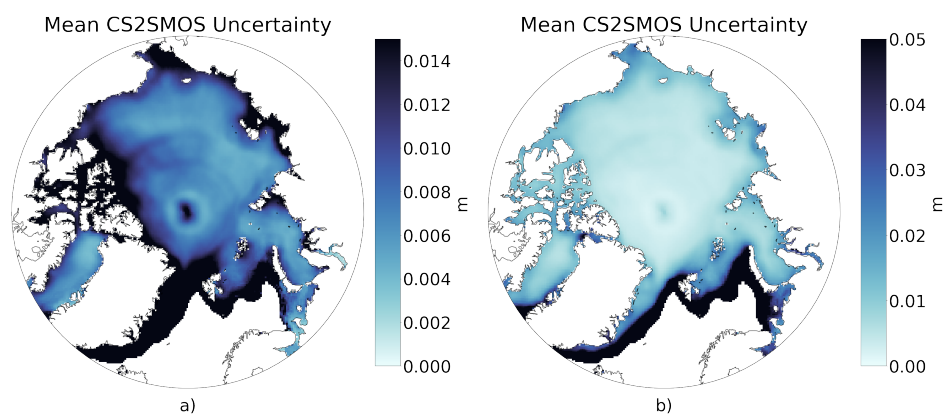
**Figure 7.** Mean AWI CS2SMOS (a) absolute uncertainty and (b) relative uncertainty during wintertime from late 2010 through early 2021 (except the winter of 2011-2012) as provided by the data product. This uncertainty is very similar in magnitude and pattern to uncertainty in dynamic effect and is mostly far below 5%.

When compared against buoy data, Anheuser et al. (2022) report SLICE to have a thermodynamic growth mean bias of $4 \times 10^{-4}$ m d$^{-1}$ and standard deviation bias of $2.2 \times 10^{-3}$ m d$^{-1}$. Calculating a standard error from this standard deviation using a total number of samples of 227 leads to an uncertainty contribution of 0.001 m wk$^{-1}$. The assumption of 2 Wm$^{-2}$ of basal flux from liquid water to solid sea ice leads to additional uncertainty from SLICE. Assuming a density of 917 kg m$^{-2}$
395    and a latent heat of fusion of 3.32 x $10^5$ J kg$^{-1}$, each 1 W m$^{-2}$ of basal sensible heat flux from the liquid sea water to solid sea ice is equivalent to a sea ice thermodynamic growth rate of $2.84 \times 10^{-4}$ m d$^{-1}$. If the assumed 2 W m$^{-2}$ basal sensible heat flux were removed, sea ice growth would increase by $5.67 \times 10^{-4}$ m d$^{-1}$ and an increase from 2 W m$^{-2}$ to 10 W m$^{-2}$

would decrease thermodynamic sea ice thickness growth by $2.27 \times 10^{-3}$ m d$^{-1}$. The SLICE thermodynamic growth retrieval also does not account for lateral melt and freeze processes.

400    A potential mechanism for error occurs in the relationship between lead frequency and the snow–ice interface retrieval results. Leads and areas of lower sea ice concentrations necessarily contain open sea water exposed at the surface. Sea water has significantly lower emissivity in the microwave band than sea ice, therefore reducing passive microwave brightness temperatures in these regions. To the extent that leads of open water covers a grid cell, these lower brightness temperature would then artificially reduce the retrieved snow–ice interface temperature and cause erroneously large thermodynamic growth rates.

405    Via Eq. 4, erroneously high thermodynamic growth without a change to the CS2SMOS estimates leads to erroneously lower dynamic effects. This phenomenon is difficult to spot because negative dynamic effects are indeed expected in regions with high lead frequency. We restrict our analysis to sea ice concentrations of greater than 95% as retrieved by established passive microwave methods. As such, the highest possible open water fraction within a grid cell is 5%. Assuming emissivity of a satellite field of view is a linear sum of scene type emissivities weighted by area fraction, the effect of 5% open water by area

410    on satellite retrieved snow–ice interface temperature can be approximated. Using an approximate open water emmissivity at 6.9 GHz of 0.56 and sea ice emissivity of 0.98, the emissivity of a 95% sea ice concentration is 0.959. This reduction in emissivity from 0.98 for a 100% sea ice concentration scene equates to a 5.25 K reduction in brightness temperatures for a 250 K snow–ice interface temperature. Propagating this difference through the retrieval algorithm per Kilic et al. (2019) leads to a reduction of retrieved snow–ice interface temperature of 6 K. In a scenario with thin ice and a small temperature gradient

415    across the ice, this difference could be significant.

    Motion vector uncertainty adds to the uncertainty in advection effect and the deformation effect calculated as a residual between dynamic effect and advection effect. Tschudi et al. (2020) lists a maximum ice motion error of 0.7 cm s$^{-1}$ which corresponds to 605 m d$^{-1}$. The contribution of this error to advection effect and deformation effect error is reduced by spatial gradients in the sea ice thickness fields being small. The highest uncertainties in advection effect are found in the Greenland

420    and Barents Seas where motion vectors and thickness gradients are largest.

## 6    Conclusions

Sea ice models, including those contained within global climate models, account for sea ice thickness and volume through separate thermodynamic and dynamic processes. These processes are affected by different mechanisms in a changing climate, meaning independent observations of each are essential for comparison with model results to ensure each process is

425    correct independently, regardless of whether overall thickness is correct. In this study, we present the first basin-wide, Eulerian, sub-seasonal temporal resolution, and long-term estimation of dynamics effect on sea ice thickness, thermodynamic sea ice thickness growth, advection effect on sea ice thickness and deformation effect on sea ice thickness. By retrieving thermodynamic sea ice thickness growth by driving a simple model with passive microwave based snow–ice interface temperature observations (Anheuser et al., 2022) and differencing this growth on a weekly basis from overall sea ice thickness growth

430    calculated from a satellite altimeter and passive microwave combination sea ice thickness product (Ricker et al., 2017b), we

estimated wintertime, basin-wide sea ice dynamic effects on a spatial and temporal scale beyond the localized and seasonal studies available to date. Using a sea ice motion product (Tschudi et al., 2020), we also separated the overall dynamic effect into its Eulerian, independent component effects of advection and deformation.

Thermodynamic growth is lowest in the central Arctic, lower than 0.04 m wk$^{-1}$, and highest in the seasonal ice zones, often greater than 0.08 m wk$^{-1}$. The highest positive dynamic effects of greater than 0.04 m wk$^{-1}$ are found north of the Canadian Arctic Archipelago, where the Transpolar Drift and Beaufort Gyre deposit ice. Strong negative dynamic effects of greater than 0.08 m wk$^{-1}$ are found where the Transpolar Drift originates. The deformation and advection effect fields are dominated by couplets with opposite sign between the two. The Beaufort Sea is characterized by positive advection effects of 0.04 m wk$^{-1}$ and negative deformation effects of similar magnitude, while most other regions are characterized by negative advection effects, sometimes as low as -0.04 m wk$^{-1}$ and positive deformation effects, often times greater than 0.04 m wk$^{-1}$. The highest dynamic effect relative to thermodynamic effect is found north of the Canadian Arctic Archipelago, where dynamics account for twice the sea ice thickness growth as thermodynamics. Similarly, deformation is highest relative to thermodynamics in these regions as well, with deformation more than doubling thermodynamics here and slightly farther north, near the North Pole. A seasonal cycle is also shown for all thickness effects effects, the most prominent feature of which is an increasing positive deformation thickness effect and overall dynamic thickness effect as the winter season progresses. A potential mechanism for this is increasing ice thickness resisting lead formation and making more ice volume available for ridging.

Yearly results compare well with a recent study of the Lagrangian dynamic and thermodynamic effects on sea ice thickness along the Multidisciplinary drifting Observatory for the Study of Arctic Climate (MOSAiC) drift track during the winter of 2019-2020. Where our data shows Lagrangian dynamics accounting for 48.7 % of growth in the grid cells nearest the drifting study area during this time period, (Koo et al., 2021) found similar results of 42.6 % over a similar spatial scale. This lends confidence in our larger spatial and temporal scale results.

The most significant source of uncertainty in all four effects, thermodynamics, dynamics, advection, and deformation, is the uncertainty in the AWI CS2SMOS sea ice thickness product. The mean uncertainty in this product over the study period is similar to the standard error in the dynamics and deformation fields. Both AWI CS2SMOS sea ice thickness and the standard error in our results have similar magnitudes and are potentially significant in the Kara, Barents and East Greenland Seas as well as most coastal regions.

Next steps for this data include further interrogation of trends and patterns. There may be a relation to atmospheric conditions or patterns like the Arctic Oscillation or trends related to the changing climate. An additional step will be comparison of these results to those given by sea ice and global climate models.

**Appendix A**

*Code and data availability.* Data used in creation of all figures is available at https://doi.org/10.5281/zenodo.7278280. Code for creation of data and figures is available at https://doi.org/10.5281/zenodo.7292123 and https://github.com/janheuser/thmdyn. The following auxiliary datasets were used and are available at these locations: AMSR-E and AMSR2 brightness temperatures, https://doi.org/10.5067/AMSR-E/AE_SI25.003 and https://doi.org/10.5067/TRUIAL3WPAUP; AMSR-E and AMSR2 SIC, https://doi.org/10.5067/AMSR-E/AE_SI25.003
465 and https://doi.org/10.5067/TRUIAL3WPAUP; AWI CS2SMOS, https://www.meereisportal.de; sea ice motion vectors, https://doi.org/10.5067/INAWUWO7QH7B; MOSAiC drift track, https://doi.pangaea.de/10.1594/PANGAEA.937193;

*Author contributions.* JA completed all analysis and wrote the first draft under guidance from YL and JK. All authors worked together towards a final draft.

*Competing interests.* The authors declare that they have no conflict of interest.

470 *Acknowledgements.* This work was funded by the National Oceanic and Atmospheric Administration (NOAA) under grant no. NA20NES4320003. The views, opinions, and findings contained in this report are those of the author(s) and should not be construed as an official National Oceanic and Atmospheric Administration or U.S. Government position, policy, or decision. The merging of CryoSat-2 und SMOS data was funded by the ESA project SMOS & CryoSat-2 Sea Ice Data Product Processing and Dissemination Service and data from November 1st, 2010 to April 1st, 2021 were obtained from https://www.meereisportal.de (grant: REKLIM-2013-04).
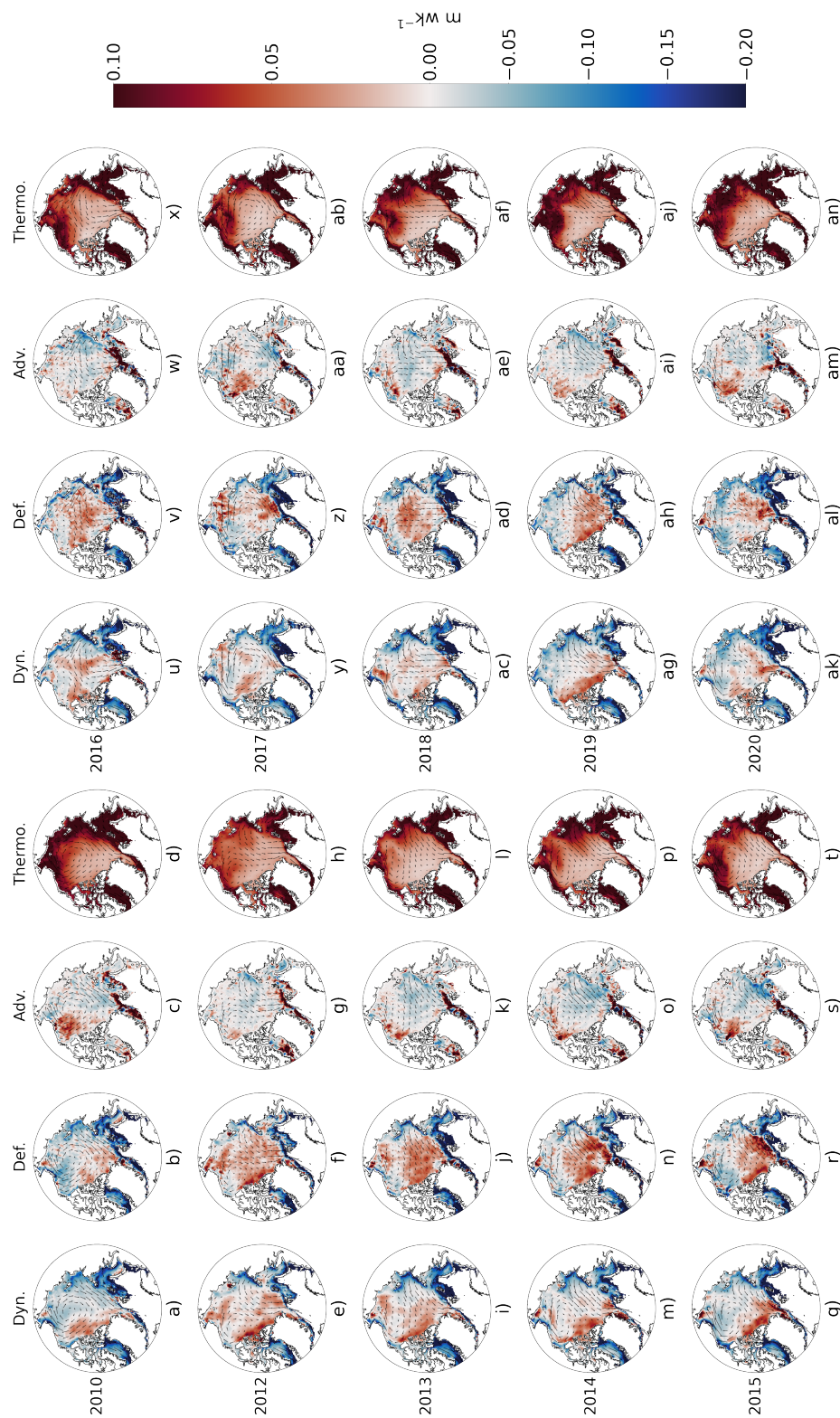
**Figure A1.** Mean dynamic, deformation, advection and thermodynamic effects for the winters beginning in 2010-2020 except 2011 with yearly mean ice motion vectors plotted. The patterns of dynamic, advective and deformation effects broadly follow the ice motion vectors.

# References

Anheuser, J., Liu, Y., and Key, J.: A simple model for daily basin-wide thermodynamic sea ice thickness growth retrieval, The Cryosphere, 16, 4403–4421, https://doi.org/10.5194/tc-16-4403-2022, 2022.

DeRepentigny, P., Tremblay, L. B., Newton, R., and Pfirman, S.: Patterns of Sea Ice Retreat in the Transition to a Seasonally Ice-Free Arctic, J. Climate, 29, 6993 – 7008, https://doi.org/10.1175/JCLI-D-15-0733.1, 2016.

Feltham, D. L., Untersteiner, N., Wettlaufer, J. S., and Worster, M. G.: Sea ice is a mushy layer, Geophysical Research Letters, 33, L14 501, https://doi.org/10.1029/2006gl026290, 2006.

Guerreiro, K., Fleury, S., Zakharova, E., Kouraev, A., Remy, F., and Maisongrande, P.: Comparison of CryoSat-2 and ENVISAT radar freeboard over Arctic sea ice: toward an improved Envisat freeboard retrieval, Cryosphere, 11, 2059–2073, https://doi.org/10.5194/tc-11-2059-2017, 2017.

Hendricks, S. and Ricker, R.: Product User Guide & Algorithm Specification: AWI CryoSat-2 Sea Ice Thickness (version 2.3), https://doi.org/10013/epic.ecd56b5d-3e7d-4a65-9019-588b1c3b0d26, 2020.

Hendricks, S., Paul, S., and Rinne, E.: ESA Sea Ice Climate Change Initiative (Sea_Ice_cci): Northern hemisphere sea ice thickness from the CryoSat-2 satellite on a monthly grid (L3C), v2.0. Centre for Environmental Data Analysis, https://doi.org/10.5285/ff79d140824f42dd92b204b4f1e9e7c2, 2018.

Hibler, W. D.: MODELING A VARIABLE THICKNESS SEA ICE COVER, Monthly Weather Review, 108, 1943–1973, https://doi.org/10.1175/1520-0493(1980)108<1943:mavtsi>2.0.co;2, hibler, wd, 1980.

Hoffman, J. P., Ackerman, S. A., Liu, Y. H., and Key, J. R.: The Detection and Characterization of Arctic Sea Ice Leads with Satellite Imagers, Remote Sensing, 11, https://doi.org/10.3390/rs11050521, 2019.

Itkin, P., Spreen, G., Hvidegaard, S. M., Skourup, H., Wilkinson, J., Gerland, S., and Granskog, M. A.: Contribution of Deformation to Sea Ice Mass Balance: A Case Study From an N-ICE2015 Storm, Geophysical Research Letters, 45, 789–796, https://doi.org/10.1002/2017gl076056, 2018.

Kilic, L., Tonboe, R. T., Prigent, C., and Heygster, G.: Estimating the snow depth, the snow–ice interface temperature, and the effective temperature of Arctic sea ice using Advanced Microwave Scanning Radiometer 2 and ice mass balance buoy data, Cryosphere, 13, 1283–1296, https://doi.org/10.5194/tc-13-1283-2019, 2019.

Koo, Y., Lei, R. B., Cheng, Y. B., Cheng, B., Xie, H. J., Hoppmann, M., Kurtz, N. T., Ackley, S. F., and Mestas-Nunez, A. M.: Estimation of thermodynamic and dynamic contributions to sea ice growth in the Central Arctic using ICESat-2 and MOSAiC SIMBA buoy data, Remote Sensing of Environment, 267, https://doi.org/10.1016/j.rse.2021.112730, 2021.

Kurtz, N. T., Galin, N., and Studinger, M.: An improved CryoSat-2 sea ice freeboard retrieval algorithm through the use of waveform fitting, Cryosphere, 8, 1217–1237, https://doi.org/10.5194/tc-8-1217-2014, 2014.

Kwok, R.: Contrasts in sea ice deformation and production in the Arctic seasonal and perennial ice zones, Journal of Geophysical Research-Oceans, 111, https://doi.org/10.1029/2005jc003246, 2006.

Kwok, R. and Cunningham, G. F.: Variability of Arctic sea ice thickness and volume from CryoSat-2, Philos. T. Roy. Soc. A, 373, 2045, https://doi.org/10.1098/rsta.2014.0157, 2015.

Kwok, R. and Cunningham, G. F.: Contributions of growth and deformation to monthly variability in sea ice thickness north of the coasts of Greenland and the Canadian Arctic Archipelago, Geophysical Research Letters, 43, 8097–8105, https://doi.org/10.1002/2016gl069333, 2016.

Laxon, S. W., Giles, K. A., Ridout, A. L., Wingham, D. J., Willatt, R., Cullen, R., Kwok, R., Schweiger, A., Zhang, J. L., Haas, C., Hendricks, S., Krishfield, R., Kurtz, N., Farrell, S., and Davidson, M.: CryoSat-2 estimates of Arctic sea ice thickness and volume, Geophys. Res. Lett., 40, 732–737, https://doi.org/10.1002/grl.50193, 2013.

515  Lepparanta, M.: A Review of Analytical Models of Sea–Ice Growth, Atmos. Ocean, 31, 123–138, https://doi.org/10.1080/07055900.1993.9649465, 1993.

Markus, T., Neumann, T., Martino, A., Abdalati, W., Brunt, K., Csatho, B., Farrell, S., Fricker, H., Gardner, A., Harding, D., Jasinski, M., Kwok, R., Magruder, L., Lubin, D., Luthcke, S., Morison, J., Nelson, R., Neuenschwander, A., Palm, S., Popescu, S., Shum, C. K., Schutz, B. E., Smith, B., Yang, Y. K., and Zwally, J.: The Ice, Cloud, and land Elevation Satellite-2 (ICESat-2): Science requirements, concept,

520  and implementation, Remote Sens. Environ., 190, 260–273, https://doi.org/10.1016/j.rse.2016.12.029, 2017.

Mecklenburg, S., Drusch, M., Kerr, Y. H., Font, J., Martin-Neira, M., Delwart, S., Buenadicha, G., Reul, N., Daganzo-Eusebio, E., Oliva, R., and Crapolicchio, R.: ESA's Soil Moisture and Ocean Salinity Mission: Mission Performance and Operations, IEEE T. Geosci. Remote., 50, 1354–1366, https://doi.org/10.1109/tgrs.2012.2187666, 2012.

Meier, W. N., Stroeve, J., and Fetterer, F.: Whither Arctic sea ice? A clear signal of decline regionally, seasonally and extending beyond the

525  satellite record, Annals of Glaciology, Vol 46, 2007, 46, 428–+, https://doi.org/10.3189/172756407782871170, 2007.

Nicolaus, M., Perovich, D. K., Spreen, G., Granskog, M. A., von Albedyll, L., Angelopoulos, M., Anhaus, P., Arndt, S., Belter, H. J., Bessonov, V., Birnbaum, G., Brauchle, J., Calmer, R., Cardellach, E., Cheng, B., Clemens-Sewall, D., Dadic, R., Damm, E., de Boer, G., Demir, O., Dethloff, K., Divine, D. V., Fong, A. A., Fons, S., Frey, M. M., Fuchs, N., Gabarró, C., Gerland, S., Goessling, H. F., Gradinger, R., Haapala, J., Haas, C., Hamilton, J., Hannula, H.-R., Hendricks, S., Herber, A., Heuzé, C., Hoppmann, M., Høyland, K. V., Huntemann,

530  M., Hutchings, J. K., Hwang, B., Itkin, P., Jacobi, H.-W., Jaggi, M., Jutila, A., Kaleschke, L., Katlein, C., Kolabutin, N., Krampe, D., Kristensen, S. S., Krumpen, T., Kurtz, N., Lampert, A., Lange, B. A., Lei, R., Light, B., Linhardt, F., Liston, G. E., Loose, B., Macfarlane, A. R., Mahmud, M., Matero, I. O., Maus, S., Morgenstern, A., Naderpour, R., Nandan, V., Niubom, A., Oggier, M., Oppelt, N., Pätzold, F., Perron, C., Petrovsky, T., Pirazzini, R., Polashenski, C., Rabe, B., Raphael, I. A., Regnery, J., Rex, M., Ricker, R., Riemann-Campe, K., Rinke, A., Rohde, J., Salganik, E., Scharien, R. K., Schiller, M., Schneebeli, M., Semmling, M., Shimanchuk, E., Shupe, M. D., Smith,

535  M. M., Smolyanitsky, V., Sokolov, V., Stanton, T., Stroeve, J., Thielke, L., Timofeeva, A., Tonboe, R. T., Tavri, A., Tsamados, M., Wagner, D. N., Watkins, D., Webster, M., and Wendisch, M.: Overview of the MOSAiC expedition: Snow and sea ice, Elementa: Science of the Anthropocene, 10, https://doi.org/10.1525/elementa.2021.000046, 2022.

Ricker, R., Hendricks, S., Helm, V., Skourup, H., and Davidson, M.: Sensitivity of CryoSat-2 Arctic sea–ice freeboard and thickness on radar-waveform interpretation, Cryosphere, 8, 1607–1622, https://doi.org/10.5194/tc-8-1607-2014, 2014.

540  Ricker, R., Hendricks, S., Kaleschke, L., and Tian-Kunze, X.: CS2SMOS User Guide v3.0, https://doi.org/10013/epic.51136, 2017a.

Ricker, R., Hendricks, S., Kaleschke, L., Tian-Kunze, X., King, J., and Haas, C.: A weekly Arctic sea-ice thickness data record from merged CryoSat-2 and SMOS satellite data, Cryosphere, 11, 1607–1623, https://doi.org/10.5194/tc-11-1607-2017, 2017b.

Stefan, J.: Ueber die Theorie der Eisbildung, insbesondere über die Eisbildung im Polarmeere, Ann. der Phy.-Berlin, 278, 269–286, https://doi.org/https://doi.org/10.1002/andp.18912780206, 1891.

545  Thorndike, A. S., Rothrock, D. A., Maykut, G. A., and Colony, R.: Thickness Distribution of Sea Ice, J. Geophys. Res.-Oc. Atm., 80, 4501–4513, https://doi.org/10.1029/JC080i033p04501, 1975.

Tian-Kunze, X., Kaleschke, L., Maass, N., Makynen, M., Serra, N., Drusch, M., and Krumpen, T.: SMOS-derived thin sea ice thickness: algorithm baseline, product specifications and initial verification, Cryosphere, 8, 997–1018, https://doi.org/10.5194/tc-8-997-2014, 2014.

Tilling, R. L., Ridout, A., and Shepherd, A.: Estimating Arctic sea ice thickness and volume using CryoSat-2 radar altimeter data, Adv. Space
550    Res., 62, 1203–1225, https://doi.org/10.1016/j.asr.2017.10.051, 2018.

Tschudi, M., Meier, W. N., Stewart, J. S., Fowler, C., and Maslanik, J.: Polar Pathfinder Daily 25 km EASE-Grid Sea Ice Motion Vectors,
Version 4, https://doi.org/10.5067/INAWUWO7QH7B, 2019.

Tschudi, M. A., Meier, W. N., and Stewart, J. S.: An enhancement to sea ice motion and age products at the National Snow and Ice Data
Center (NSIDC), Cryosphere, 14, 1519–1536, https://doi.org/10.5194/tc-14-1519-2020, 2020.

555   von Albedyll, L., Haas, C., and Dierking, W.: Linking sea ice deformation to ice thickness redistribution using high-resolution satellite and
airborne observations, CRYOSPHERE, 15, 2167–2186, https://doi.org/10.5194/tc-15-2167-2021, 2021.

von Albedyll, L., Hendricks, S., Grodofzig, R., Krumpen, T., Arndt, S., Belter, H. J., Birnbaum, G., Cheng, B., Hoppmann, M., Hutchings,
J., Itkin, P., Lei, R. B., Nicolaus, M., Ricker, R., Rohde, J., Suhrhoff, M., Timofeeva, A., Watkins, D., Webster, M., and Haas, C.: Ther-
modynamic and dynamic contributions to seasonal Arctic sea ice thickness distributions from airborne observations, Elementa-Science of
560   the Anthropocene, 10, https://doi.org/10.1525/elementa.2021.00074, 2022.

Willmes, S. and Heinemann, G.: Sea-Ice Wintertime Lead Frequencies and Regional Characteristics in the Arctic, 2003-2015, Remote
Sensing, 8, https://doi.org/10.3390/rs8010004, 2016.

Wingham, D. J., Francis, C. R., Baker, S., Bouzinac, C., Brockley, D., Cullen, R., de Chateau-Thierry, P., Laxon, S. W., Mallow, U.,
Mavrocordatos, C., Phalippou, L., Ratier, G., Rey, L., Rostan, F., Viau, P., and Wallis, D. W.: CryoSat: A mission to determine the
565   fluctuations in Earth's land and marine ice fields, Natural Hazards and Oceanographic Processes from Satellite Data, 37, 841–871,
https://doi.org/10.1016/j.asr.2005.07.027, 2006.

Zhang, J. L. and Rothrock, D.: A thickness and enthalpy distribution sea-ice model, Journal of Physical Oceanography, 31, 2986–3001,
https://doi.org/10.1175/1520-0485(2001)031<2986:ataeds>2.0.co;2, 2001.